Hualien Ridge: A tectonic ridge transitioning from plate collision to subduction

Lien-Kai Lin [a], Shu-Kun Hsu [a,*], Ching-Hui Tsai [b], Yi-Ching Yeh [a], Shiou-Ya Wang [a,b], Kuan-Ting Chen [a], Song-Chuen Chen [c], Hsiao-Shan Lin [b]

[a] *Department of Earth Sciences, National Central University, Taiwan*
[b] *Center for Environmental Studies, National Central University, Taiwan*
[c] *Central Geological Survey, New Taipei City, Taiwan*

ARTICLE INFO

ABSTRACT

The Longitudinal Valley in eastern Taiwan is generally considered as a collisional suture between the Philippine Sea and the Eurasian plates. Offshore to the northeast of the valley, the Philippine Sea Plate is subducting beneath the Ryukyu Arc. The corner between eastern Taiwan and the Ryukyu Arc system is therefore the transition from plate collision to plate subduction. In consequence, the area has complicated tectonics and frequent earthquakes. In this study, we used marine geophysical data to study the submarine Hualien Ridge that is situated in this plate collision/subduction transition zone. Our results show that the Hualien Ridge is tectonically divided into the active southern part and the inactive northern part. In the southern Hualien Ridge, we find several ~N30°E trending active faults and some could be linked to the active faults in the onshore Milun Tableland. The structures in the southern Hualien Ridge and the Milun Tableland display a pop-up structure that is subject to the oblique compression from the northwestward motion of the Philippine Sea Plate. The ~N30°E trending faults are the results of the transpressional system. However, the Milun Fault, the western boundary of the fault system, probably terminates near 24°03′N, where a pronounced bathymetric depression trending N300° cuts across the whole Hualien Ridge. In fact, all the active faults in the southern Hualien Ridge only appear to the south of the bathymetric depression. In contrast, in the northern Hualien Ridge we only find blind normal faults covered by ~100 m thick sediments. The distinct variation of tectonic activity in the Hualien Ridge underlines the transition from the active collision to inactive collision or partial subduction of the Philippine Sea Plate relative to the Eurasian Plate.

1. Introduction

The junction corner between the Ryukyu and Taiwan islands is a transition zone between the subduction of the Philippine Sea Plate beneath the Eurasian Plate and the collision of the two plates (e.g. Angelier, 1990; Hsu et al., 1996; Lallemand et al., 2001; Hsu, 2001a; Malavieille et al., 2002; Sibuet and Hsu, 2004; Wu et al., 2009a, 2009b; Wang et al., 2019). Located in eastern Taiwan, the Longitudinal Valley is generally considered as a collisional suture between the Philippine Sea and the Eurasian plates (e.g. Teng, 1990; Hsu and Sibuet, 1995; Lee et al., 1998, 2001; Shyu et al., 2005) (Fig. 1). The northern end of the Longitudinal Valley is adjacent to the westernmost Ryukyu subduction system (e.g. Biq, 1981; Liu et al., 1998; Shyu et al., 2005; Chen et al., 2014; Shyu et al., 2016; Shyu et al., 2020; Wang et al., 2019). On the other hand, due to the waning of the collision, the northwestward sub-duction of the Philippine Sea Plate has caused the fast southward migration of the southern Ryukyu Arc and the fast opening of the southern Okinawa Trough (e.g. Sibuet et al., 1998; Hsu, 2001b; Chen et al., 2018). In consequence, the geologic structures are complex and earthquakes are numerous in the junction area between Taiwan and Ryukyu islands (Kao et al., 1998; Theunissen et al., 2012; Hsiao et al., 2014; Wang et al., 2019) (Fig. 1). The main geologic features from the onshore to the offshore area of this corner are the northern Longitudinal Valley, the Milun Tableland, the Hualien Ridge and the Shincheng Ridge (Fig. 1).

Earthquake focal mechanisms of the study area show that the regional stress is in the NW-SE direction and compressive (Kao et al., 1998; Kuochen et al., 2004; Wu et al., 2009a, 2009b; Huang et al.,
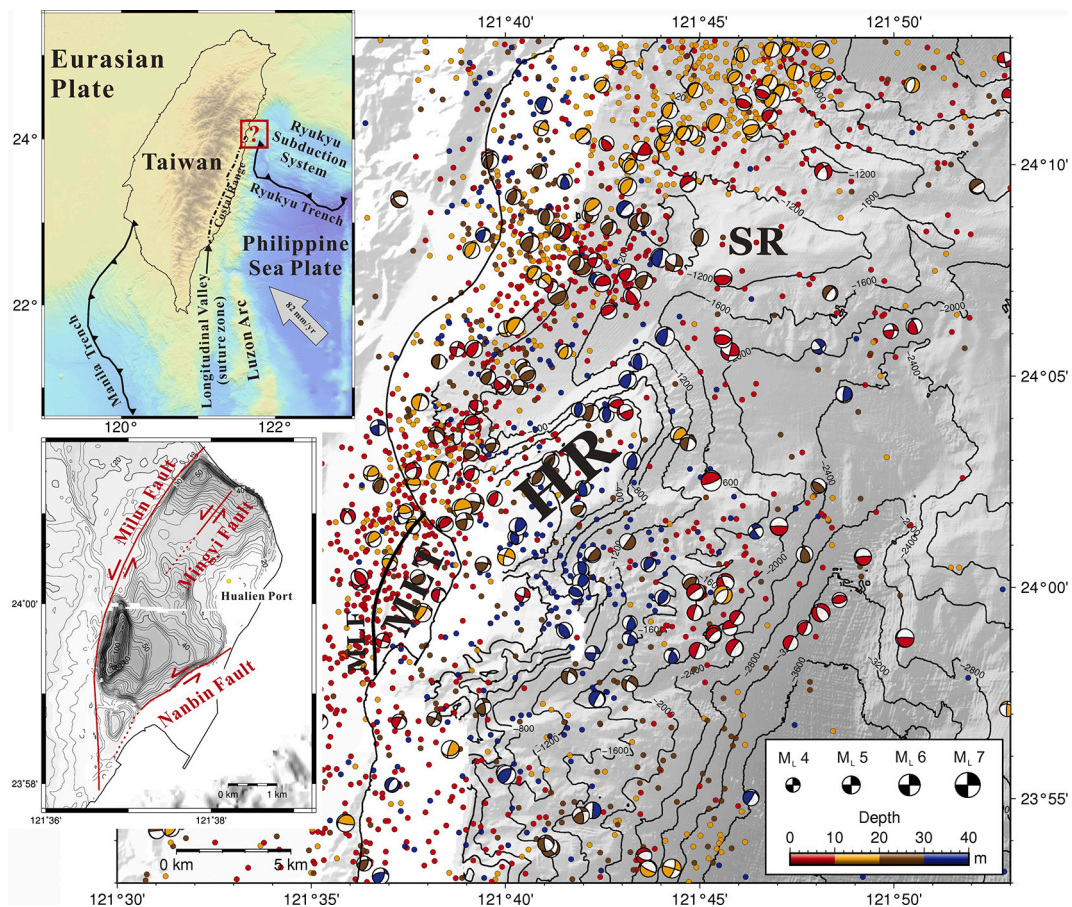

Fig. 1. Tectonic background, bathymetry, background seismicity and earthquake focal mechanisms of the study area. (Left upper panel) The study area is located in the northernmost Longitudinal Valley and is adjacent to the southwesternmost Ryukyu subduction system. (Right panel) From south to north, the geological units are the Milun Tableland (MLT), the Hualien Ridge (HR), and the Shincheng Ridge (SR). The Milun Tableland is generally considered as a pop-up structure related to left-lateral strike-slip faults, including Milun Fault, Mingyi Fault, and Nanbin Fault. The traces of the Mingyi Fault and Nanbin Fault are from Lin and Hsiao (1998). The trace of the Milun Fault is based on the Central Geological Survey reports (Chung et al., 2004). The seismicity and focal mechanisms from 1995 to 2014 are from the earthquake catalog of Wu et al. (2008) and their later compilations.

2012). Because of the oblique convergence, the northern portion of the Coastal Range and the Longitudinal Valley are subject to a left-lateral strike-slip stress (Yu et al., 1997; Yu and Kuo, 2001; Ching et al., 2011; Chen et al., 2014). Fig. 1 shows the seismicity and focal mechanisms from 1995 to 2014 from the earthquake catalog of Wu et al. (2008) and their further compilations. In this compilation, the magnitudes of the earthquakes are greater than three. Because the Wadati-Benioff zone beneath the northern Longitudinal Valley could reach about 40 km deep (Shyu et al., 2016), we only adopted the earthquakes less than 40 km deep. However, the focal depths of the earthquakes beneath the Milun Tableland are generally less than 10 km (Fig. 1).

In the northern end of the Coastal Range, the Milun Tableland and Milun Fault are two main geologic features (Fig. 1). The Milun Tableland is bordered by the Milun Fault in the west. The Milun Fault is an active fault that ruptured in October 1951 and February 2018 (Yang, 1953; Hsu, 1955, 1962; Lin, 1957, 1962, Yu, 1997; Lin and Hsiao, 1998; Chung et al., 2004; Lin et al., 2019; Huang et al., 2019; Hsu et al., 2019; Yen et al., 2019). Based on field investigations, the co-seismic vertical offset across the surface rupture was about 1.2 m and the left-lateral offsets was about 2 m during the M7.3 earthquake in October 1951 (Hsu, 1955, 1962; Lin, 1957, 1962; Yu, 1997; Lin and Hsiao, 1998). The 1951 earthquake occurred in the northward extension of the Milun Fault and the focal mechanism displayed a left-lateral motion (Cheng et al., 1997). Likewise, field investigations shows that the M_w 6.4 earthquake in 2018 caused an uplift of ~50 cm and a left-lateral offset of ~60 cm along the Milun fault (Yu et al., 1990; Ching et al., 2011; Yen et al., 2011; Chen

et al., 2014). A seismic profile across the Milun Fault shows that the Milun Fault is a sub-vertical fault with high angle southeast-dipping plane (Liao, 2006). To the east of the Milun Fault about 1 km, the Mingyi Fault was associated with a M7.3 earthquake in October 1951 (Yang, 1986; Yu, 1994; Lin and Hsiao, 1998). A seismic profile indicates that the Mingyi Fault has also a sub-vertical fault plane (Liao, 2006). However, the southward extension of the Mingyi Fault is still debated. According to the previous studies, there is a N40°E west-dipping Nanbin Fault along the Nanbin cliff in the southeast of the Milun Tableland (Lin, 1962; Yu, 1994; Lin and Hsiao, 1998). After the 1951 Hualien earthquake, the tide height dropped about 50 cm on average in the inner harbor of the Hualien Port, which is the upthrown side of the Nanbin Fault (Fig. 1). In other words, the west of the Nanbin Fault was uplifted during the 1951 Hualien earthquake. (Yu, 1994; Lin and Hsiao, 1998). In general, the Milun Tableland is considered as a pop-up structure associated with left-lateral strike-slip faults (Fig. 1).

However, due to the lack of offshore data, the structures of the northward continuation of the Milun Fault and the Milun Tableland are unknown, especially in the area of the submarine Hualien Ridge. To have a comprehensive understanding of the transitional structures between collision and subduction, we study the tectonics and seabed features of the Hualien Ridge by using Multi-beam bathymetric data, side-scan sonar images (SSS), and sub-bottom profiles (DBP), high-resolution single channel (SCSPK) and multi-channel (MCSPK) sparker seismic reflection profiles and conventional multi-channel air-gun seismic reflection (MCS) profiles (Fig. 2).
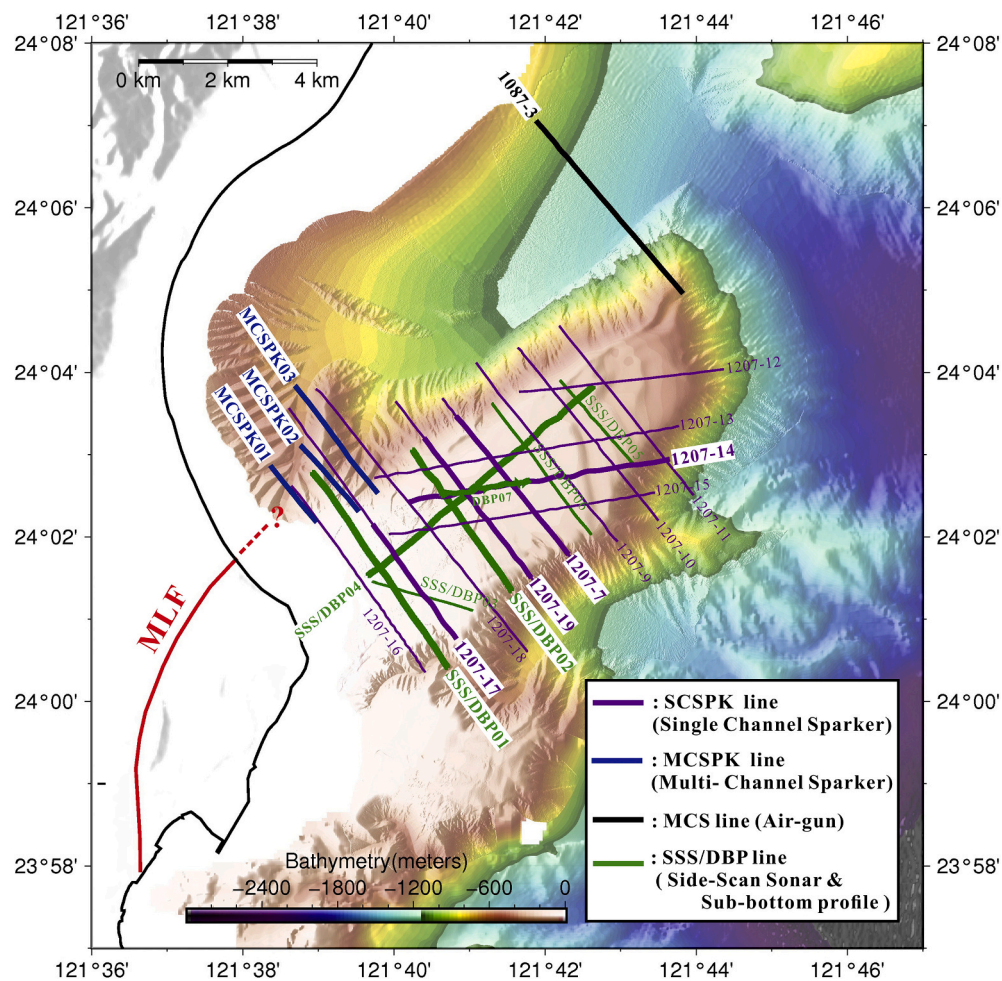
Fig. 2. The distribution of the survey lines used in this study. The green lines indicate 6 deep-towed side-scan sonar and sub-bottom profiler data. The purple lines indicate the locations of 12 Sparker seismic profiles. The black and deep blue lines indicate the locations of one multi-channel air-gun seismic and 3 multi-channel Sparker seismic profiles. MLF: Milun Fault. (For interpretation of the references to colour in this figure legend, the reader is referred to the web version of this article.)

2. Data acquisition and processing

Multi-beam bathymetric data were collected onboard the R/V Ocean Research 2 by using the Atlas MD50 bathymetric data acquisition system during the cruise OR2–2179 in July 2016 and the R/V New Ocean Research 2 by using the Kongsberg EM712 bathymetric data acquisition system during the cruise NOR2–0014 in October 2020 (Fig. 2). Six deep-towed side scan sonar profiles from SSS01 to SSS06 and chirp (sub-bottom profiler) profiles from DBP01 to DBP06 were also collected during the cruise OR2–2179 in July 2016 (Fig. 2). DBP07 was collected during the cruise OR1–1207 in September 2018. The side scan sonar is of dual frequencies of 120 and 410 kHz, which provide resolutions of 6.25 cm and 1.9 cm, respectively. The sub-bottom profiler is operated at 0.5–7 kHz, giving a maximum vertical resolution of 15 to 25 cm. The deep-towed equipment was generally operated at 30–50 m above the seafloor with 2–3 knots survey speed.

In order to understand deeper structures, we acquired high-resolution reflection seismic data across the Hualien Ridge with air-gun or sparker sources. All the seismic profiles in this study were processed by using Paradigm Echos seismic processing software. Three multichannel seismic profiles (MCS) were collected by seismic data acquisition system onboard R/V Ocean Research 1 during the cruise OR1–1087 in September 2014 (Fig. 2). The air-gun source has a volume of 625 cube inches and was triggered every 20 s at a vessel speed of 4–5 knots. Seismic signals were received by a 24-channel streamer and the recording length is 8 s with 1 ms sample rate. The group interval is 6.25

m. Two MCS profiles were filtered with a 4–8–60-120 Hz band-pass filter to suppress noise. The pre-stack spiking/predictive deconvolution was applied with 120 ms operator length, the period between primary pulse and bubble pulse. The predictive length to remove the bubble effect is 18 ms. The normal move out correction and post-stack migration in F-K domain were performed using a constant water velocity of 1500 m/s.

There are twelve profiles of single channel sparker seismic data (SCSPK) collected by DELPH seismic data acquisition system during the cruise OR1–1207 in September 2018 (Fig. 2). We used a sparker source of 6 kJ, shot every 4 s at a vessel speed of 2–3 knots, which is about 5 m shot interval with respect to the seafloor. Simultaneously, seismic signals were received by a fluid-type single channel streamer with a 0.25 ms sampling rate. The other three solid type multi-channel sparker seismic profiles (MCSPK) collected by the Geode seismic data acquisition system during the cruise NOR2–0014 in October 2020. A solid type 24 channel streamer was deployed and received signal with 3.125 m channel interval and 0.25 ms sampling rate. The MCSPK datasets were processed by following steps: SEG-D data input, geometry definition and CMP calculation, zero-phase band-pass frequency filter, source signature deconvolution, spiking/predictive deconvolution, de-ghost, de-multiple, trace balance, spherical divergence correction, normal move out correction based on velocity analysis (NMO), CMP residual static correction, post-stack Kirchhoff time migration, minimum phase band-pass filter, SEG-Y format data output and plotting. Each sparker seismic profile was filtered with a 60–180-480-640 Hz zero-phase band-pass filter to suppress random noise. However, due to the instabilities
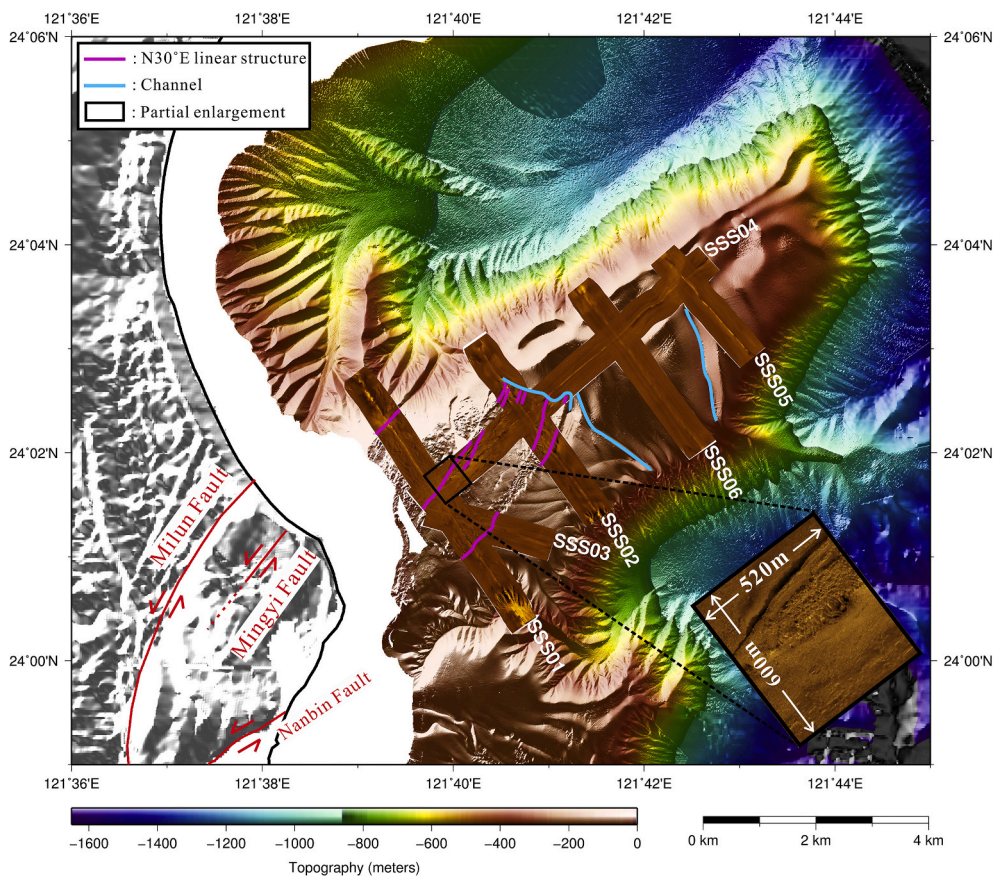
Fig. 3. The side-scan sonar images and the ~N30°E linear structures (indicated by purple lines) in the southern Hualien Ridge. The side-scan sonar images are overlapped on the bathymetry. The width of each side-scan sonar image is 600 m. The N30°E linear features also exist on the western slope of the Hualien Ridge. The bathymetric channels across the Hualien Ridge are marked by blue colour. (For interpretation of the references to colour in this figure legend, the reader is referred to the web version of this article.)

and unrepeatable of the sparker source, the sparker source waveform is not a minimum phase. Hence, all sparker seismic profiles were applied the source signature deconvolution before the further processing. We also made the residual static correction on the NMO-corrected gathers to correct the water bottom time difference due to the swell height. Finally, we applied a 60–120–240-480 Hz minimum phase band-pass filter to eliminate the noise produced by the processing and enhance the signal. The single channel datasets (SCSPK) were processed using a similar workflow.

3. Tectonic interpretations

3.1. N30°E linear structures in southern Hualien Ridge

Based on the bathymetry and side scan sonar images of the Hualien Ridge, we can identify several sub-linear structures trending N30°E on the seafloor (pink lines in Fig. 3). Similar bathymetric features trending N30°E also appear at the western slope of the Hualien Ridge, particularly the feature that can connect the linear structure in the northwest side of Profile SSS01 (Fig. 3). Based on the sub-bottom profiles DBP01, DBP02 and DBP04, we interpret those N30°E trending features on the seafloor as faults (Figs. 3, 4 and S1). As shown in profiles DBP01 and DBP02, some faults display sub-vertical dipping and even crop out on the seafloor (F1, F3, F5 and F6 in Fig. 4a; F4, F5, F6 and F7 in Fig. 4b), while some are blind faults that do not propagate up across an unconformity (F3, F8 and F9 in Fig. 4b). A sliding normal fault F10 in the slope is covered by ~50 m thick sediments (Fig. 4b). Generally, the eastern

portion of the Hualien Ridge is covered by thicker sediments than the summit area (Fig. 4b). Profile DBP04 is along the NE-SW trend of the Hualien Ridge and cuts across profiles DBP01 and DBP02 (see locations in Fig. 2). The near-seafloor structures in profile DPB04 show that the southern Hualien Ridge has been faulted and uplifted, whereas the northern Hualien Ridge is tectonically inactive and overlain by thick drifted sediments (Fig. 4c). It is noteworthy that those roughly N30°E faults or sub-linear structures are oblique to the general NE-SW trend of the Hualien Ridge and only outcrop on the southwestern portion of the Hualien Ridge. The deep structures of the faults can be found in the sparker seismic profiles 1207–17, 1207–19, 1207–14 and 1207–7 (Figs. 5, 6, 7 and 9).

In the sparker seismic profile 1207–17, a high-angle southeast-dipping fault appear in the northwestern part of the profile, while several almost vertically northwest-dipping faults appear in the southeastern part of the profile (Fig. 5). Faults F3 and F4 outcrop on the seafloor near the crest of the southern Hualien Ridge (Fig. 5). Based on sparker seismic profile 1207–19, faults F9 and F10 are overlain by sediments below an unconformity (Fig. 6); moreover, a sliding seems to have occurred along Fault F10. Generally, a down-slope sliding is favored by a steep slope angle. For instance, the top of a steep hanging wall of reverse or transpressional fault. Slumping along the near vertical fault plane due to the gravity loading has been observed at the Milun Tableland and the other transpressional faults in New Zealand (Ameen, 1990; Eusden et al., 2005; Tseng, 2019). As shown in Fig. 7, from fault Fc to fault Fh the hanging walls have slid along a sliding surface and the dipping angles of the fault planes have decreased eastward. Particularly, these faults are

a.

b.

c.
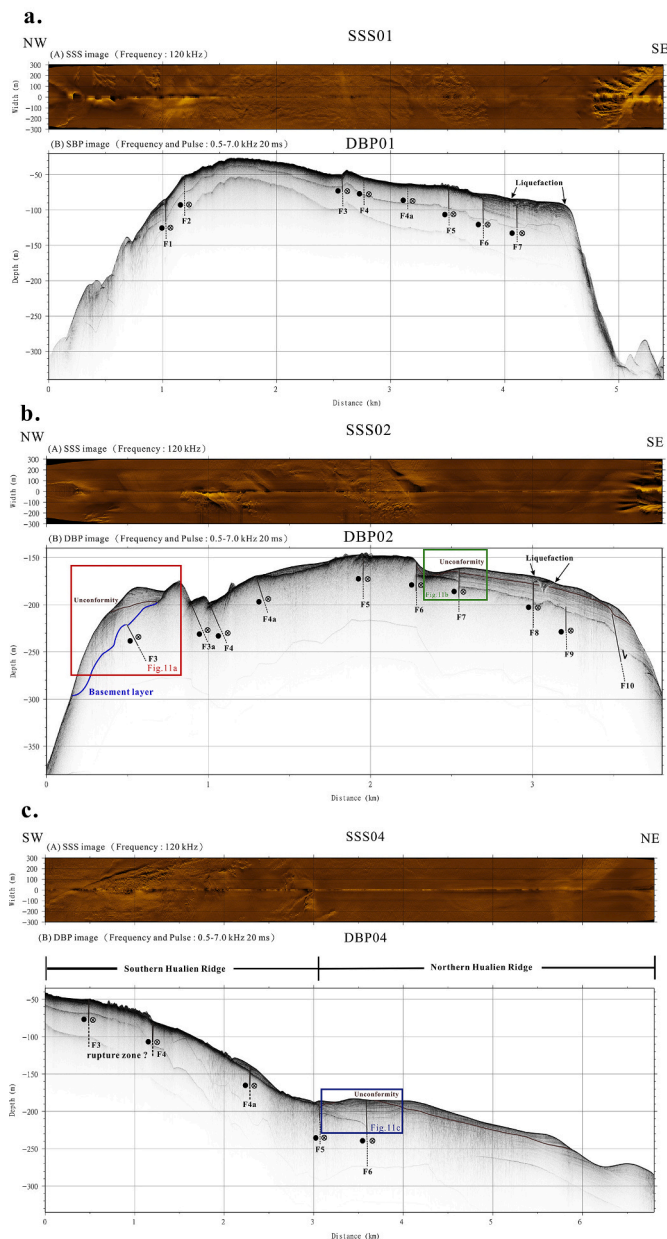
Fig. 4. Three side scan sonar images and sub-bottom chirp profiler in the Hualien Ridge (see locations in Fig. 2). Some faults outcrop on the seafloor, while some are blind faults. It is noteworthy that the axial portion of the Hualien Ridge are barely covered by sediments. Liquefactions are found on tops of faults F7 and F8. The red, green and blue boxes indicate the data that are used to perform the flattening interpretation in Fig. 11. (For interpretation of the references to colour in this figure legend, the reader is referred to the web version of this article.)

covered by thick and unbroken sediments, implying they are not active any more. We have collected sub-bottom profile DBP07 along a segment of profile 1207–14 (Fig. 7). DBP07 clearly shows that faults F4a, F5 and F6 outcrop on the seafloor but fault Fc is covered by unbroken sediments (Fig. 8). From fault Fh to fault F6 in Fig. 7, the faults are gradually covered by less and young sediments, indicating that the activity of the faults has increased westward. Now, probably due to the surface erosion or fault activity, the faults only outcrop on the western Hualien Ridge (Figs. 7 and 8). As shown in Fig. 9, the northern Hualien Ridge only contains blind normal faults covered by ~100 m thick sediments. A possible scenario showing that blind normal fault Fa may come from an inversion of a thrust fault is illustrated in the upper right panel of Fig. 9.

Running perpendicularly across the southern Hualien Ridge, the images of sub-bottom profiles DBP01 and DBP02, and sparker seismic profiles SPK-1207-17 and SPK1207–19 all indicate that the axial portion of the Hualien Ridge has been uplifted (Figs.4, 5 and 6). All the N30°E trending faults on the DBP profiles can correlate with the SPK profiles. As mentioned previously, the uncertainty of the sparker datasets could produce a little bit amplitude inconsistency in the same reflector. Therefore, we defined the accurate fault locations by using sub-bottom profiles (DBP) and connected those faults by the single channel sparker seismic profiles (SCSPK).

Fault F6 appears on the seafloor (Figs. 4c and 8). Based on sub-bottom profiles DBP04 and DBP07, fault F6 is active because the block to the south of this fault is continuously uplifting. As shown in profile DBP02, fault F7 also shows the characteristics of a growth fault (Figs. 4b and 11b). Fault F7 is therefore active. However, fault F7 does not appear in the DBP 04 (Fig. 4c), probably because fault F7 only occurs in the southern Hualien Ridge (Figs. 5 and 6). As mentioned previously, the activity of the faults in the Hualien Ridge has propagated westward. Therefore, those faults to the west of F7 could be all active (Fig. 10). Likewise, fault F3 is an active and growth fault (Figs. 4b and 11). Based on Sparker seismic profiles 1207–17 (Fig. 5), fault F2 is interpreted as a high-angle southeast-dipping active fault. Although fault F2 is covered by ~40 m thick sediments, we can still observe that the block to the east of fault F2 is uplifting (Fig, 5). Fault F1 is situated in the northeastward extension of the Mingyi Fault in the Milun Tableland (Fig. 10). The Mingyi Fault has ruptured in 1951 (Yang, 1986; Yu, 1994; Lin and Hsiao, 1998). Morphologically, the southern and northern Hualien ridges have different seafloor patterns (Figs. 3 and 10). The seafloor in the southern ridge is relatively rough and along some N30°E trending faults the seafloor seems to be covered by gravel. In contrast, the seafloor in the northern ridge is much smoother and covered by relatively fine sediments. Besides, we can observe seabed liquefaction on top of fault F8 in the southern Hualien Ridge. Thus, fault F8 is also considered as an active fault (Fig. 4b).

Overall, active faults in the Hualien Ridge only occur in the southern ridge. We delineate those faults that outcrop on the seafloor in thick red lines, and the faults that do not outcrop on the seafloor in grey lines (Fig. 10). The outcropping active faults only occur in the southern ridge, roughly to the south of the bathymetric depression indicated by the blue dashed line in Fig. 10. The southern Hualien Ridge behaves like a pop-up structure with an active ~N30°E-striking transpressional fault system (Fig. 10).

3.2. Persistent uplifting of the southern Hualien Ridge

The active uplifting of the southern Hualien Ridge reflects that the current tectonic activity of the region. As evidenced by the active faulting along the Milun Fault, Mingyi Fault and Nanbin Fault, the tectonic unit of the Milun Tableland and the southern Hualien Ridge is under an active compressional stress due to the collision of the Philippine Sea Plate (Fig. 10). In contrast, since no active faults are found in the northern Hualien Ridge, the collision of the Philippine Sea Plate should have changed to subduction or partial subduction. To better understand the uplifting history of the southern Hualien Ridge, we used the IHS Kingdom software to perform the flattening horizon interpretation. We found clear unconformities in the shallow seabed along profiles DBP02 and DBP04 (Fig. 4). The unconformities might be associated with the sea-level lowstand during last glacial period. However, due to seabed erosion on the axial portion of the Hualien Ridge and the lack of sedimentary layer dating, we were not able to correlate the sequence boundaries of the profiles. Thus, we only performed individual flattening horizon interpretations across faults F3, F6 and F7, so that we can understand the active uplifting of the southern Hualien Ridge (Figs. 4 and 13).

There are two angular unconformities in the northwestern side and southeastern side of profile DBP02, respectively (Figs. 4b, 11a and b). In
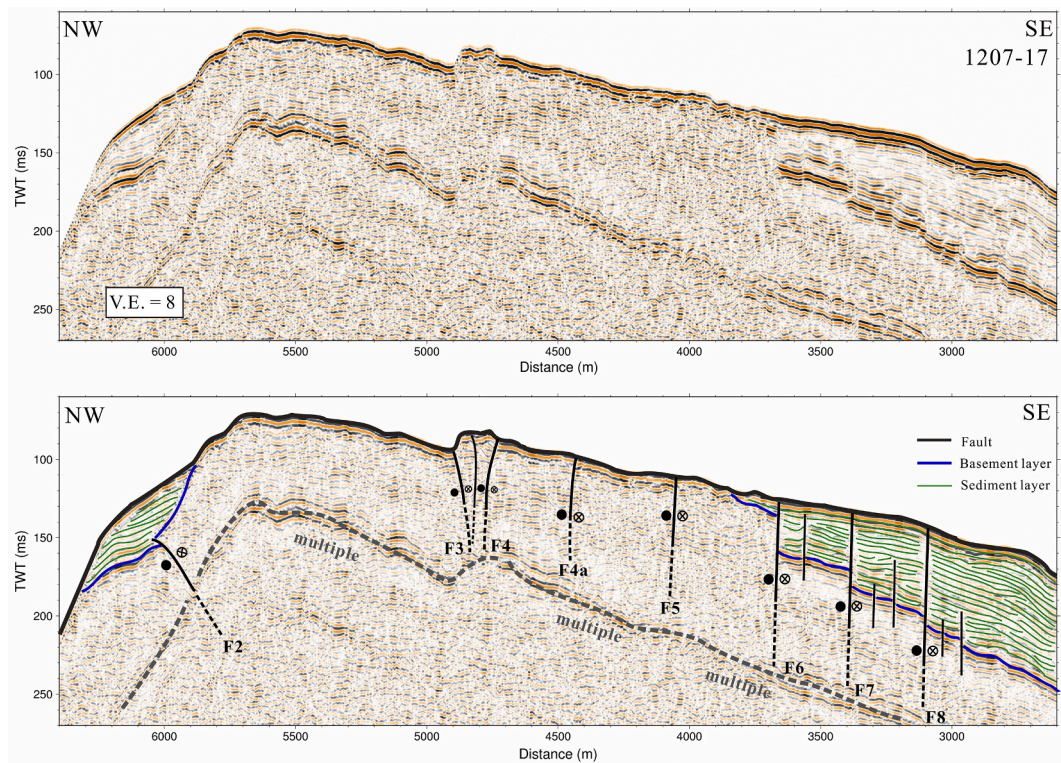
Fig. 5. Single channel sparker reflection seismic profile 1207–17 (see location in Fig. 2). Note that the southeastward dipping faults are located in the northwest side and the northwestward dipping faults are located in the southeast side.
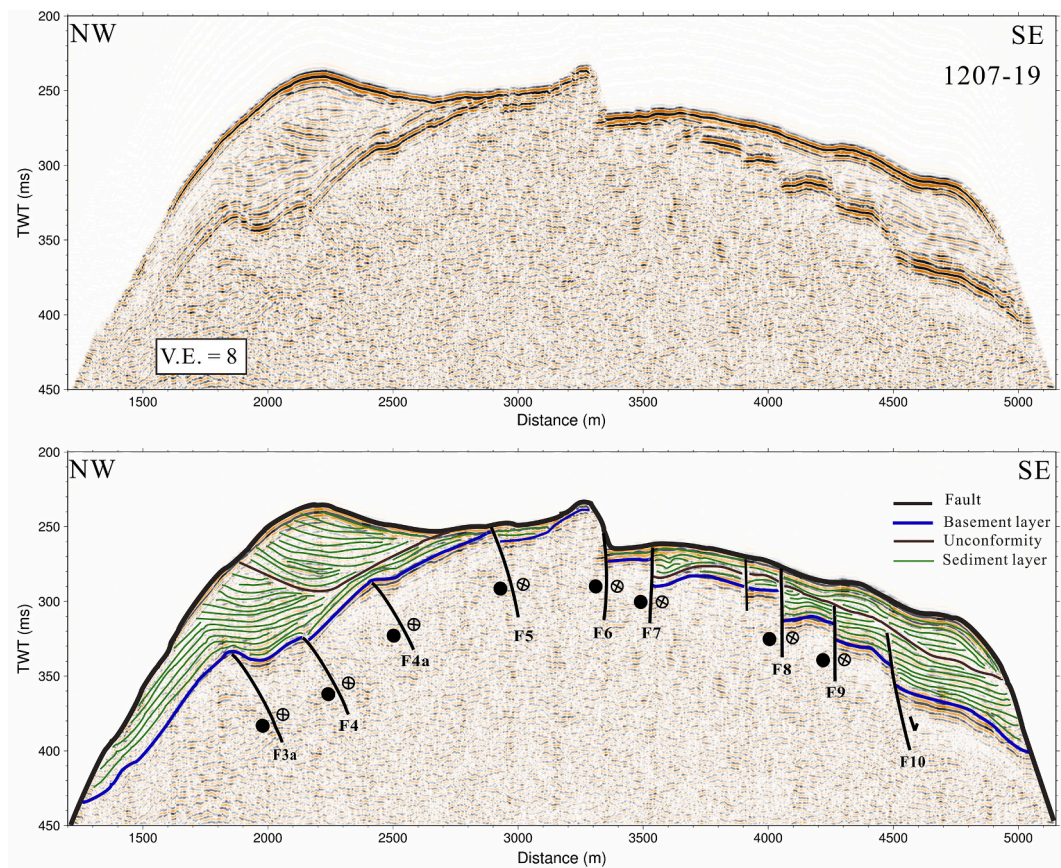

Fig. 6. Single channel sparker reflection seismic profile 1207–19 (see location in Fig. 2). Note that the near vertical northwest-dipping faults are overlain by sediments below an unconformity. Fault F10 indicates a (sliding) normal fault covered by ~100 m thick sediments.
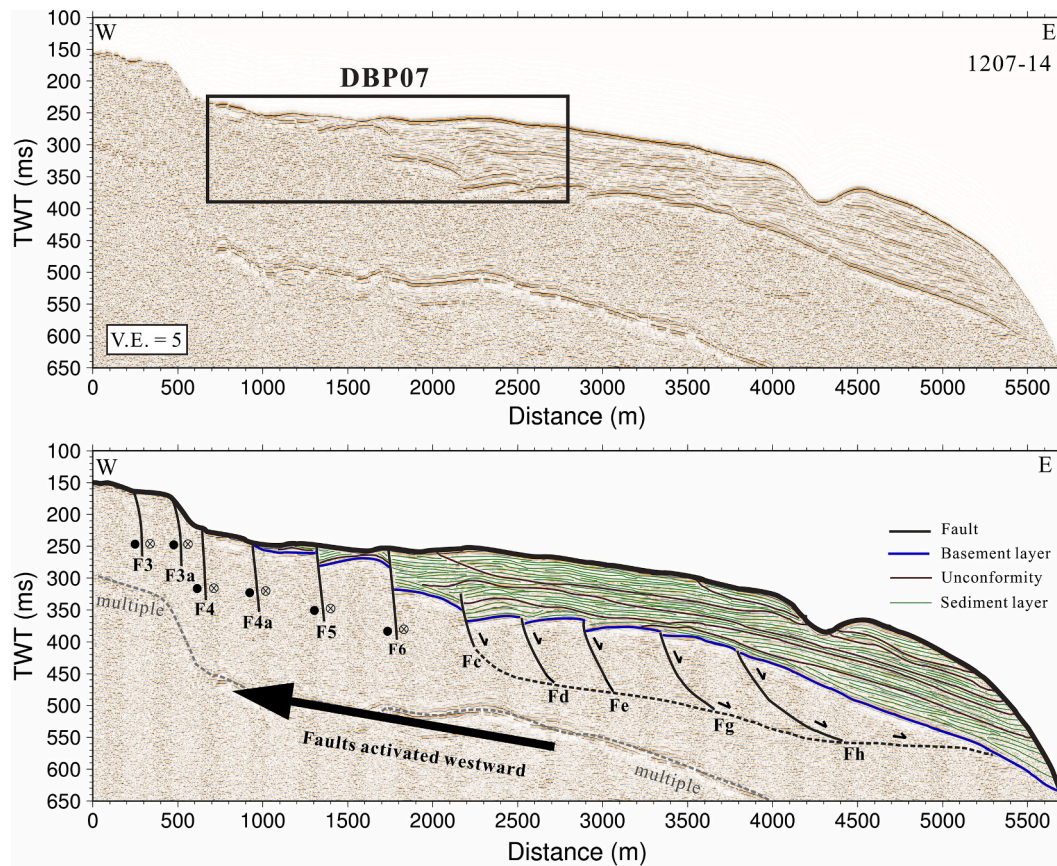
Fig. 7. Single channel sparker seismic reflection profile 1207–14 (see location in Fig. 2). It is noteworthy that from fault Fc to fault Fh the dipping angles are decreasing and overlying sediments are gradually older, suggesting that the faults were activated westward.

the northwestern side of profile DBP02, the unconformity is marked N—U1 in Fig. 11a. Due to the uplifting, most of the strata between sequence boundary N1 to unconformity N—U1 were uplifted. However, probably due to a marine regression the top layers to the east of fault F3 were eroded and the unconformity N—U1 was formed (Fig. 11a). Persistent uplifting has caused the unconformity N—U1 to tilt northwestward. On the other hand, in the southeastern side of profile DBP02, the unconformity is marked S—U1 in Fig. 11b. Due to the uplifting, most of the strata to the west of fault F7 were uplifted and tilted. However, probably also due to a marine regression the top layers to the west of fault F7 were eroded and the unconformity S—U1 was formed (Fig. 11b). Because unconformity S—U1 was cut by fault F7 and the fault outcrops on the seafloor, the uplift in the upthrown side of fault F7 should be ongoing at present. Based on our flattening horizon interpretation of profile DBP02, the southern Hualien Ridge is continuously uplifting and the uplifting has mainly occurred near the ridge axis.

Across fault F6 in profile DBP04 (Figs. 4c and 11c), we can use four sequence boundaries (T1 to T4) to constrain the uplift history of the Hualien Ridge. At stage 1, the strata below T1 deposited horizontally on both sides of fault F6. However, at stage 2 the strata between T1 and T2 were uplifted, but the layers in the southwestern side were partially eroded. Likewise, at stages 3 and stage 4 from T2 to T3 and from T3 to T4 the strata were continuously uplifted but also partially eroded in the

southwestern side of fault F6. Our reconstruction suggests that the southern Hualien Ridge may have been deformed during several uplifting events. On the other hand, to the northeast of fault F6, the sedimentary layers are almost parallel and horizontal, indicating that the northern Hualien Ridge may be tectonically stable.

3.3. Offshore extension of the Milun Fault

Since the Hualien Ridge is topographically the northeastward continuation of the Milun Tableland, the structures in the Milun Tableland could be extended to the southern Hualien Ridge. Because the regional stress is compressional in the NW-SE direction and is oblique to the Milun Tableland and the Hualien Ridge (Kao et al., 1998; Kuochen et al., 2004; Wu et al., 2009a, 2009b; Huang et al., 2012; Yu et al., 1997; Yu and Kuo, 2001; Ching et al., 2011; Chen et al., 2014), the N30°E fault system and the pop-up structure of the southern Hualien Ridge and the Milun Tableland are associated with a left-lateral transpressional stress from the plate convergence.

In October 1951 and February 2018, two earthquakes of Mw 7.3 and Mw6.4 respectively occurred in the offshore area of the Milun Fault. Both earthquakes have induced surface ruptures along the Milun Fault and caused large damages (Lin et al., 2019; Huang et al., 2019; Hsu et al., 2019; Yen et al., 2019; Lee et al., 2019). Yen et al. (2019) reported
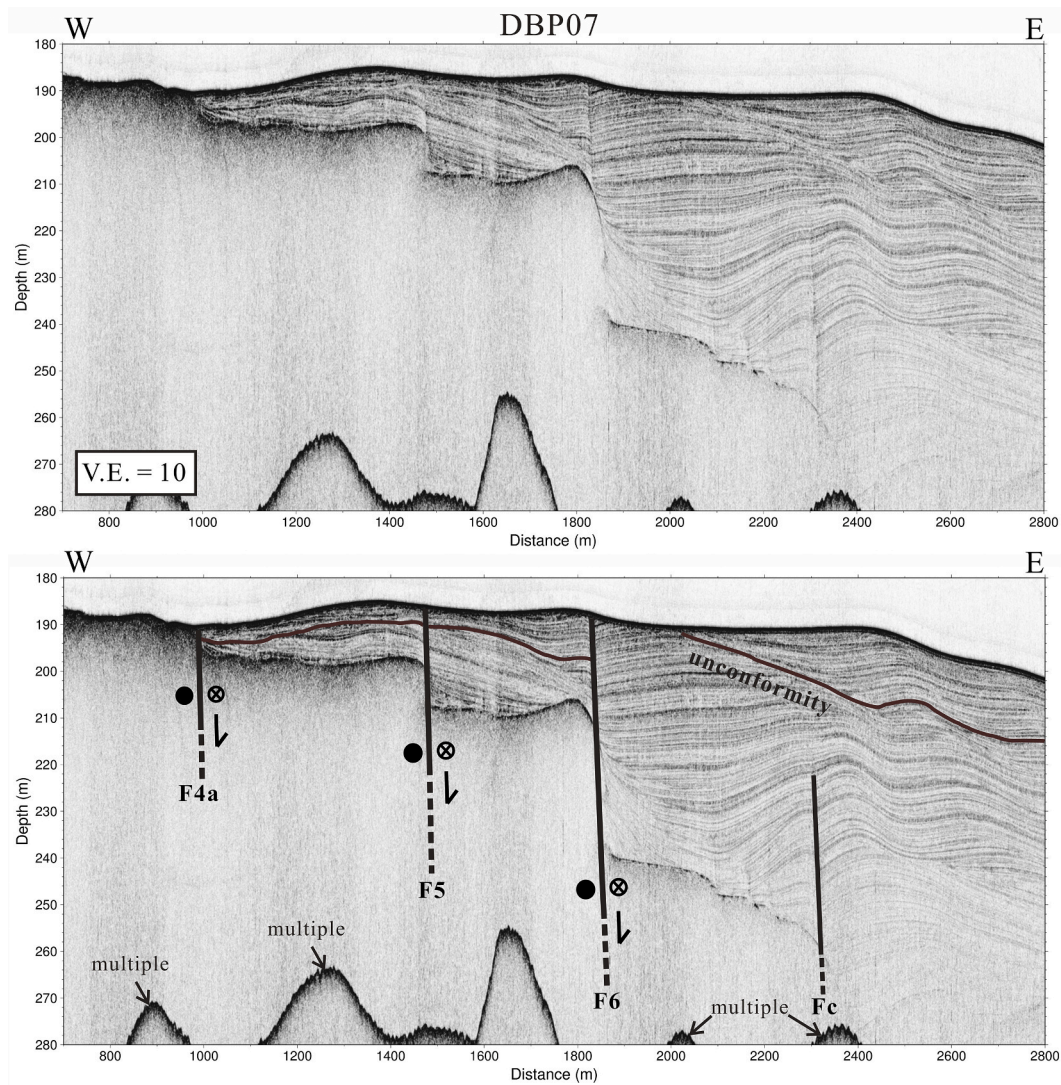
Fig. 8. The uninterpreted (upper) and interpreted (lower) sub-bottom profiles of DBP07 (see location in Figs. 2 or 7). The faults F4a, F5 and F6 outcropping on the seafloor are interpreted as active faults, but the blind fault Fc does not propagate up across an unconformity and is therefore not active.

that the 2018 Mw6.4 Hualien earthquake has produced about 70 cm of left-lateral horizontal displacement and 50 cm of uplift across the Milun Fault. Moreover, the Milun Tableland uplifted up to 45 cm and moved northeastward about 50 cm during the earthquake. However, their 3D displacement model results suggest that a model of the simple fault geometry could not explain the observed deformation. Based on our results, the co-seismic rupture of the 2018 Mw6.4 Hualien earthquake probably occurred not only on the Milun fault, but also involving the ~ N30°E fault system in the southern Hualien Ridge (Fig. 10). Although the Milun Fault is just one of the faults in this N30°E fault system, it is probably the most active fault of this transpressional left-lateral strike-slip fault system and is likely the left boundary fault of this pop-up structure.

Along the trace of the Milun Fault in the N30°E direction, the bathymetry decreases sharply to about 400 m (Fig. 10). To understand the offshore extension of the Milun Fault, we surveyed conventional air-gun multi-channel seismic line. However, the research vessel could not sail much close to the coast. The single channel sparker seismic profiles could not resolve the structure image well beneath the slope. Therefore, we collected three multi-channel sparker seismic profiles across the N30°E trace of the Milun Fault extension (Figs. 2 and 12). Onshore seismic reflection profiles across the Milun Fault showed the Milun Fault is a high-angle reverse faults dipping 60° to the east (Liao, 2006). Based on the MCSPK01 profile, a reverse fault exists in the western foot of the southern Hualien Ridge (Fig. 12a). This reverse fault also dips about 60° to the east and outcrops on the seafloor. We suggest that this reverse fault could connect with the Milun Fault (Fig. 10). In fact, we can find the trace of this fault further north in profiles MCSPK02 and MCSPK03 (Fig. 12). Based on the MCSPK02, an east-dipping reverse fault exists in the western slope of the Hualien Ridge, but is covered by mass transported deposits (Fig. 12b). Based on the MCSPK03, the fault appears beneath a valley and is covered by thicker mass transported deposits (Fig. 12c).

Based only on bathymetry, Shyu et al. (2005) suggested the offshore
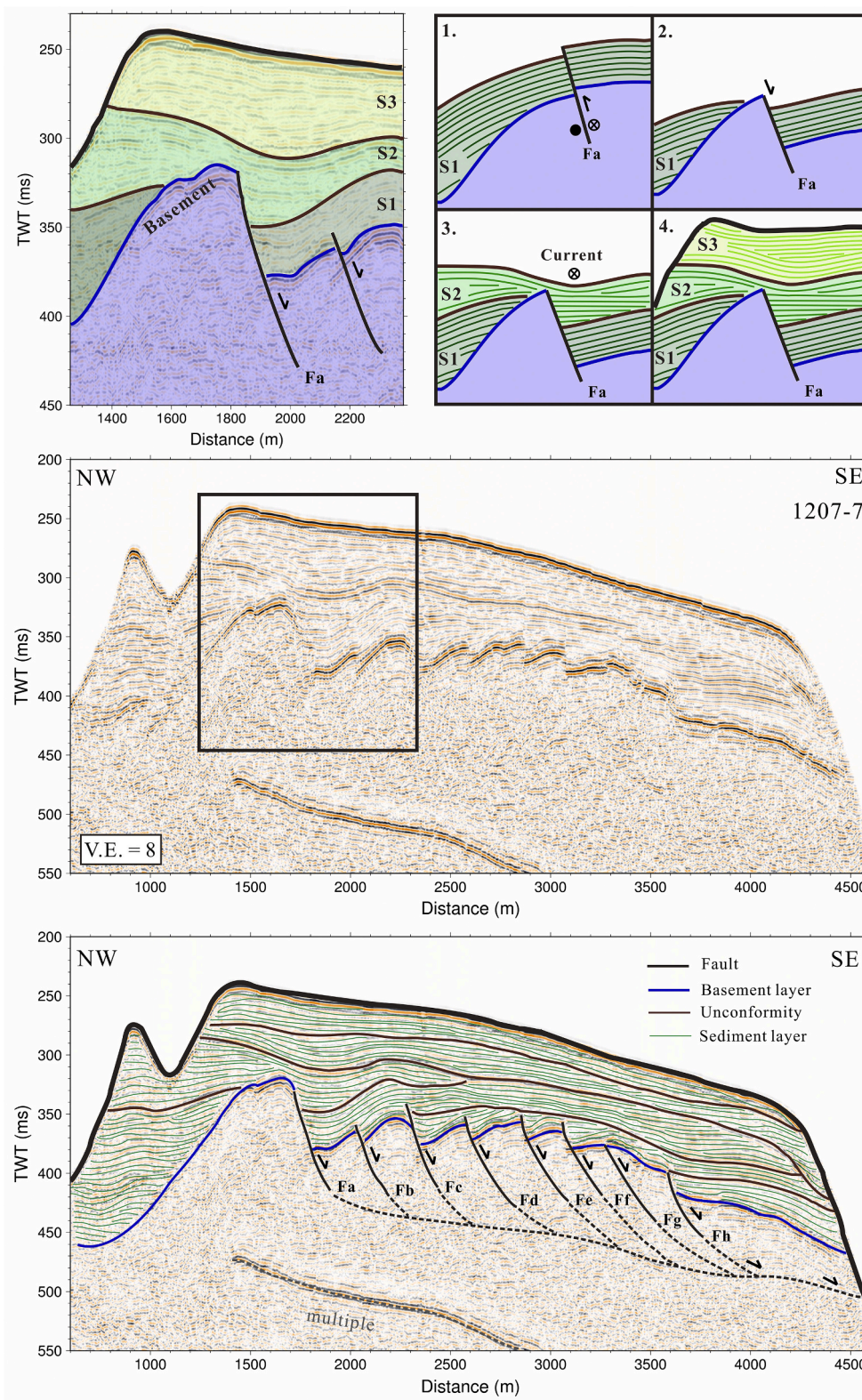
Fig. 9. Sparker seismic profile 1207–7 (middle panel) and its interpreted profile (lower panel). The basement is covered by ~150 m thick sediments. The blind faults Fa to Fh are inactive. Upper panels show a possible scenario of normal fault Fa inverted from a thrust fault; step 1 indicates a thrust fault Fa; step 2 indicates that fault Fa was inverted to a normal fault; step 3 indicates that strata S2 deposited horizontally on strata S1 with an unconformity and the fault became inactive during the S2 period; step 4 indicates that strata S3 is deposited on strata S2 with another unconformity.
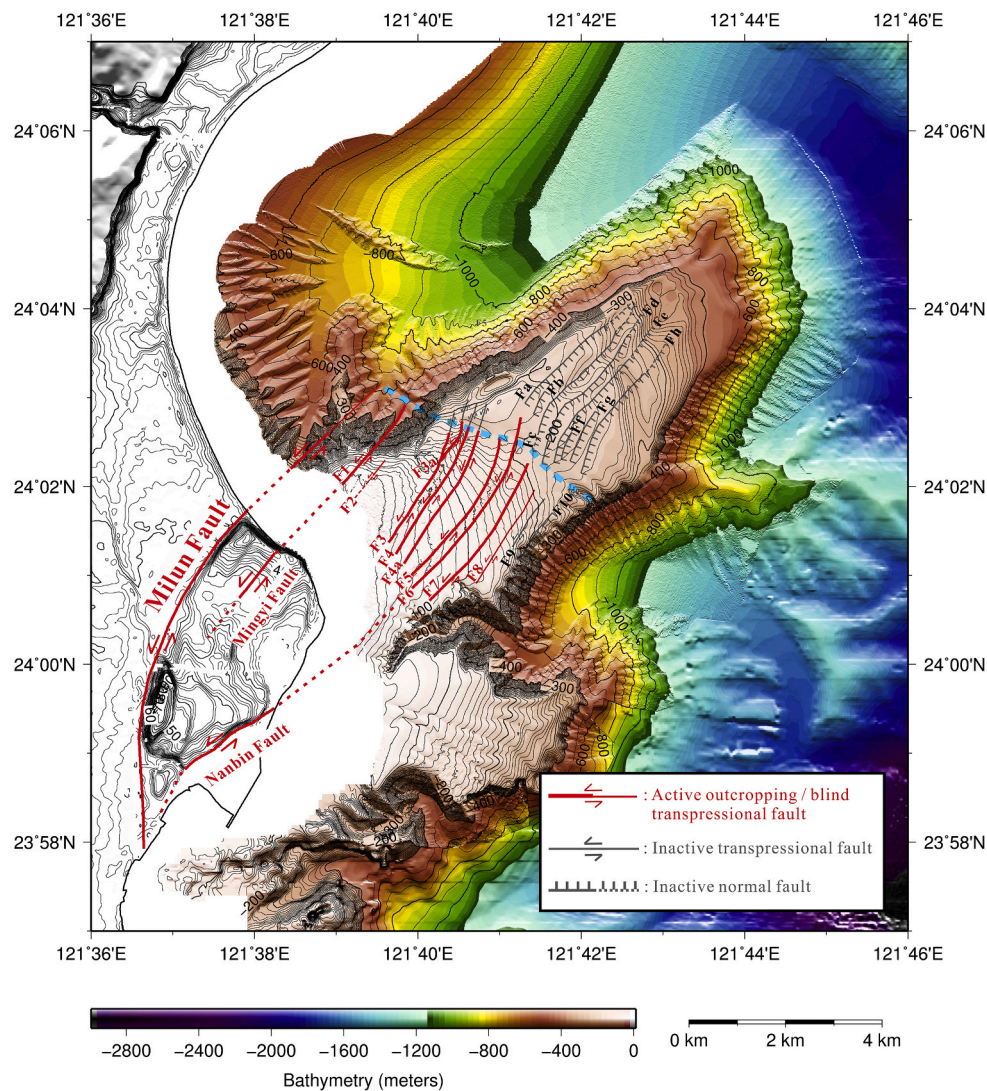
Fig. 10. Our interpreted structural map in the Hualien Ridge and Milun Tableland. The outcropping faults are delineated by thick red lines and the blind faults are delineated by dashed lines. The blue dashed line indicates a bathymetric depression that separates the southern Hualien Ridge from the northern Hualien Ridge. (For interpretation of the references to colour in this figure legend, the reader is referred to the web version of this article.)

extension of the Milun Fault could be along the whole western flank of the Hualien Ridge. However, the MCS profile 1087–3 across the western flank and foot of the northern Hualien Ridge actually show that the shallow crust is not faulted (Fig. 13). Furthermore, a N300° trending linear bathymetric high is present near 24°4.5′N and 121°39.5′E, and it is almost perpendicular to the N30°E fault system in the southern Hualien Ridge (Fig. 12). We suggest that the Milun Fault and its offshore extension, as well as all the active faults in the southern Hualien Ridge, may be limited to the south of this N300° trending bathymetric high, or even more probably only to the south of the N300° trending bathymetric depression in Fig. 10 (i.e. the blue dashed line in Fig. 10). In other words, the bathymetric boundary between the southern Hualien Ridge and the northern Hualien Ridge marks the transition from the active plate collision to the inactive collision or partially subduction.

4. Conclusions

We used bathymetric data, sub-bottom profiles, SPK profiles, and MCS profiles to investigate the tectonic structures of the Hualien Ridge, the offshore extension of the Milun Tableland. We conclude the following four main points:

(1) Tectonically, the Hualien Ridge can be divided into the active southern Hualien Ridge and the inactive northern Hualien Ridge. The difference of tectonic activity may represent the transition from the active plate collision to the inactive collision or partially subduction of the Philippine Sea Plate.
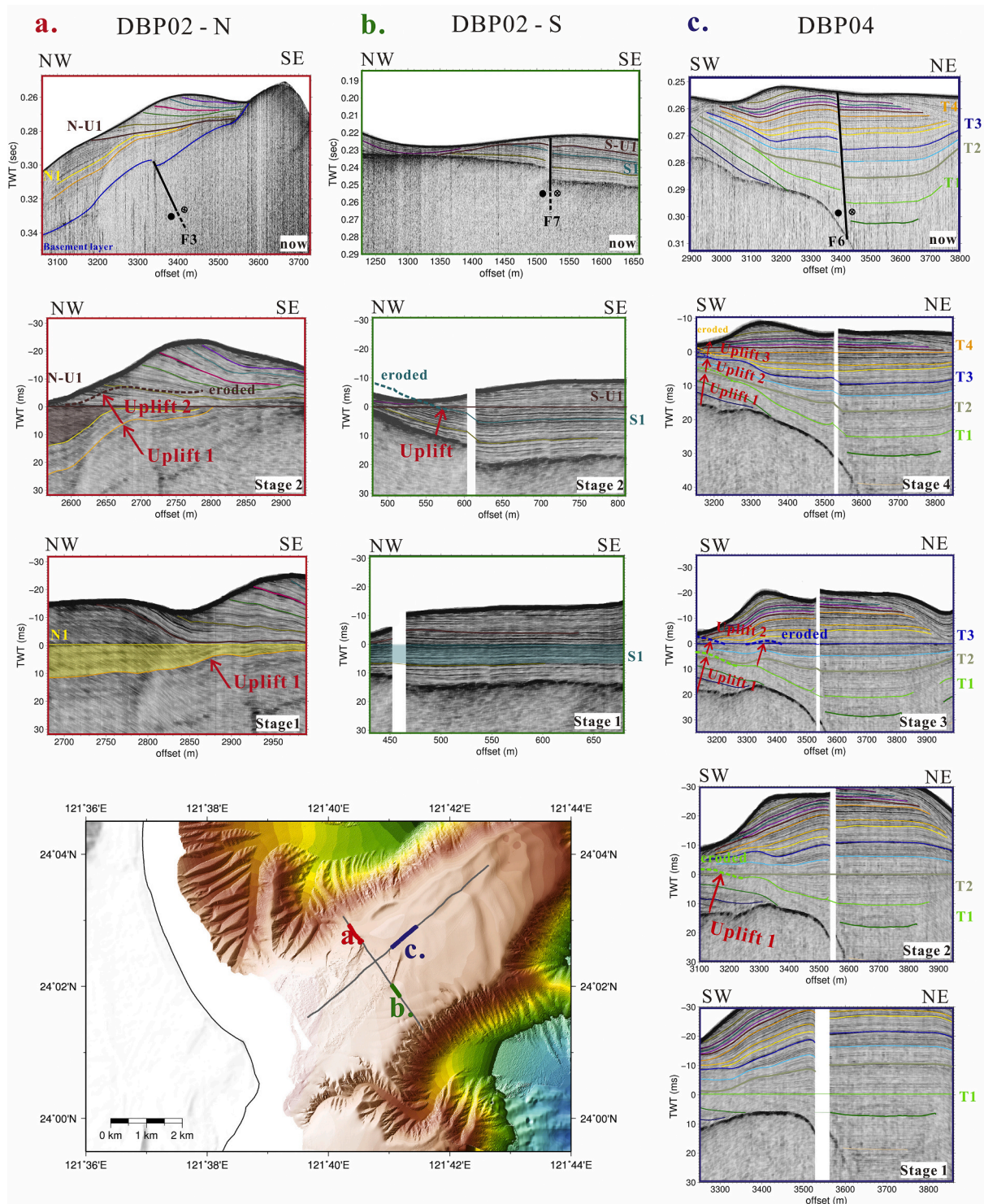
Fig. 11. The sequence boundary interpretation and flattening interpretation of profiles DBP02 and DBP04. (a). In profile DBP02-N, the strata between sequence boundary N1 and unconformity N—U1 were eroded, and the southeastern side of fault F3 was uplifted. (b). In profile DBP02-S, the strata between S1 and S—U1 were also eroded, and the northwestern side of fault F7 was uplifted. (c). In profile DBP04, four sequence boundaries were used to constrain the deposition history. In stage 1, the strata have deposited horizontally before T1. At stage 2 the strata between T1 and T2 in the southern Hualien Ridge were eroded, because the southern Hualien Ridge was uplifted. At stage 3 and stage 4, the strata between T2 and T3 and the strata between T3 and T4 were eroded in the southern Hualien Ridge, because the southern Hualien Ridge was uplifted.
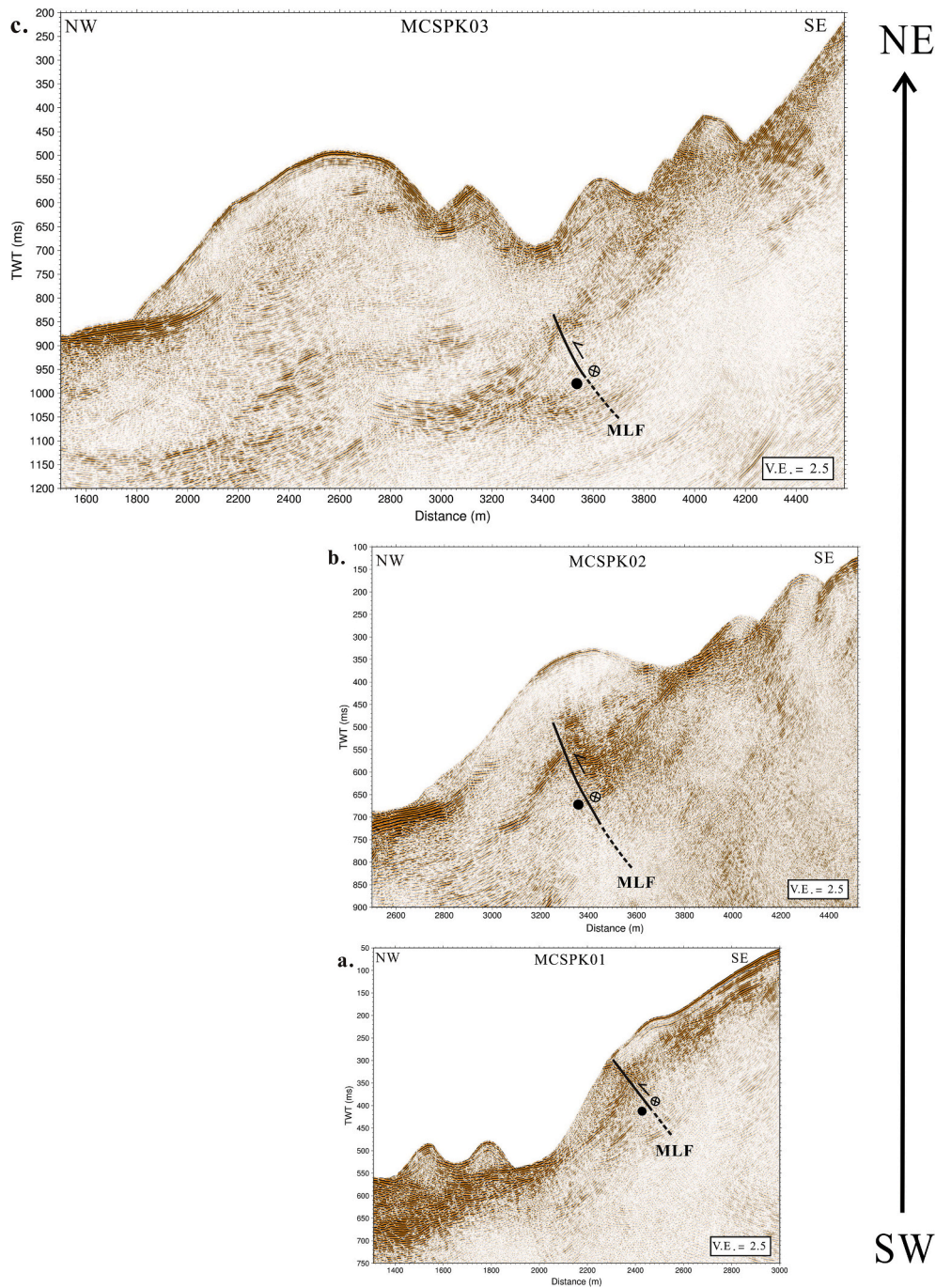
Fig. 12. MCSPK seismic profiles MCSPK01, MCSPK02 and MCSPK03 are situated in the offshore extension of the Milun Fault (see locations in Fig. 2). The east-dipping reverse fault shown in each profile confirms the offshore existence of the Milun Fault (MLF).

(2) The boundary between the southern Hualien Ridge and the northern Hualien Ridge is marked by a ~ N300° trending bathymetric depression.

(3) In terms of structure, the southern Hualien Ridge is the offshore extension of the Milun Tableland. The southern Hualien Ridge and the Milun Tableland display a pop-up structure that is subject to an oblique compression due to the northwestward collision of the Philippine Sea plate.

(4) A ~ N30°E transpressional fault system is associated with the pop-up structure. The Milun Fault is the western boundary of this fault system and probably terminates near 24°03′N.

Supplementary data to this article can be found online at https://doi.org/10.1016/j.tecto.2021.229010.

Declaration of Competing Interest

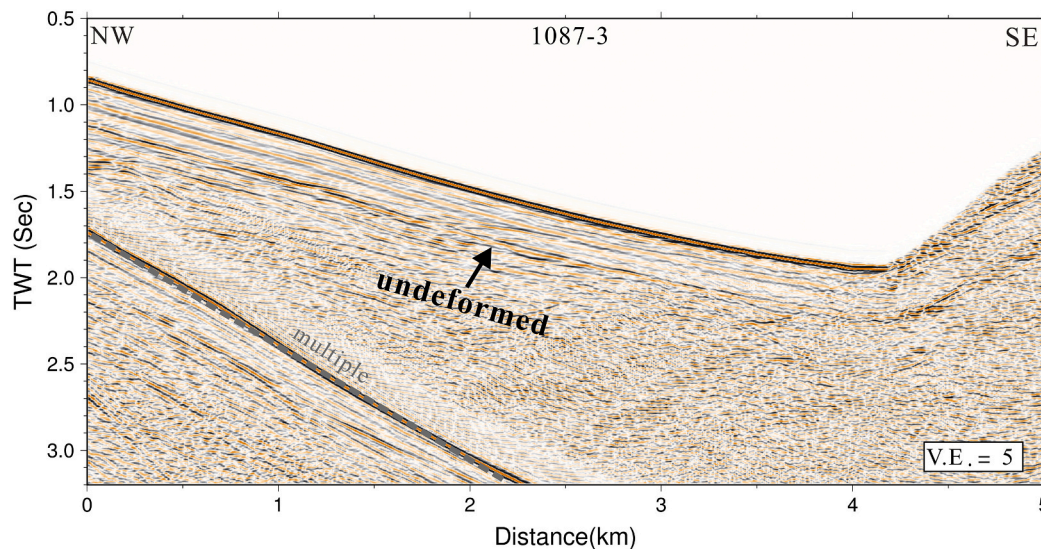The authors declare that they have no known competing financial

Fig. 13. MCS seismic profile 1087–3 is across the western slope of the northern Hualien Ridge and no clear thrust is found in this profile (see location in Fig. 2).

References

Ameen, M.S., 1990. Macrofaulting in the Purbeck-Isle of Wight Monocline. Proc. Geol. Assoc. 101, 31–46.

Angelier, J., 1990. Geodynamic Evolution of the Eastern Eurasian Margin (Foreword). Tectonophysics 83 (VII-X).

Biq, C., 1981. Collision, Taiwan-style. Mem. Geol. Soc. China 4, 91–102.

Chen, C.Y., Lee, J.C., Chen, Y.G., Chen, R.F., 2014. Campaigned GPS on present-day crustal deformation in northernmost Longitudinal Valley preliminary results, Hualien Taiwan. Terr. Atmos. Ocean. Sci. 25, 337–357.

Chen, H.-Y., Ikuta, R., Lin, C.-H., Hsu, Y.-J., Kohmi, T., Wang, C.-C., Ando, M., 2018. Back-arc opening in the western end of the Okinawa Trough revealed from GNSS/ Acoustic Measurements. Geophys. Res. Lett. 45, 137–145. https://doi.org/10.1002/ 2017GL075724.

Cheng, S.N., Yu, T.T., Yeh, Y.T., Chang, Z.-S., 1997. Relocation of the 1951 Hualien, Taitung earthquake sequence, conference on weather analysis and forecasting. Proceedings of Marine Meteorology and Seismology. In: Commemoration of 100 Years of Weather Observation in the Taiwan Area, pp. 690–699.

Ching, K.E., Hsieh, M.L., Johnson, K.M., Chen, K.-H., Rau, R.J., Yang, M., 2011. Modern vertical deformation rates and mountain building in Taiwan from precise leveling and continuous GPS observations, 2000–2008. J. Geophys. Res. 116, B08406.

Chung, L.H., Shih, T.S., Liu, Y.C., Hsu, W.L., Hsieh, C.M., Wu, W.T., 2004. Active Fault Investigation Report – Milun Fault. Central Geological Survey MOEA, Taiwan (in Chinese).

Eusden, J.D., Pettinga, J.R., Campbell, J.K., 2005. Structural collapse of a transpressive hanging-wall fault wedge, Charwell region of the Hope Fault, South Island, New Zealand. N. Z. J. Geol. Geophys. 48 (2), 295–309.

Hsiao, N.-C., Lin, T.-W., Hsu, S.-K., Kuo, K.W., Shin, T.-C., Leu, P.-L., 2014. Improvement of earthquake locations with the Marine Cable Hosted Observatory (MACHO) offshore NE Taiwan. Mar. Geophys. Res. 35 (3), 327–336.

Hsu, S.-K., 2001a. Subduction/collision complexities in the Taiwan-Ryukyu junction area: Tectonics of the northwestern corner of the Philippine Sea plate. Terr. Atmos. Ocean. Sci. 209–230.

Hsu, S.-K., 2001b. Lithospheric structure, buoyancy and coupling across the southernmost Ryukyu subduction zone: an example of decreasing plate coupling. Earth Planet. Sci. Lett. 186, 471–478.

Hsu, S.-K., Sibuet, J.-C., 1995. Is Taiwan the result of arc-continent or arc-arc collision? Earth Planet. Sci. Lett. 136 (3–4), 315–324.

Hsu, S.-K., Sibuet, J.-C., Monti, S., Shyu, C.-T., Liu, C.-S., 1996. Transition between the Okinawa trough backarc extension and the Taiwan collision: new insights on the southernmost Ryukyu subduction zone. Mar. Geophys. Res. 18 (2–4), 163–187.

Hsu, T.L., 1955. The earthquakes of Taiwan. Quart. J. Bank Taiwan 7, 39–63 (in Chinese).

Hsu, T.L., 1962. Recent faulting in the Longitudinal Valley of eastern Taiwan. Memoir Geol. Soc. China 1, 95–102.

Hsu, Y.-C., Chang, C.-P., Yen, J.-Y., Kuo-Chen, H., Wang, C.-C., 2019. Investigating the structure of the Milun Fault from surface ruptures of the 2018 Hualien Earthquake. Terr. Atmos. Ocean. Sci. 30, 337–350.

Huang, H.-H., Shyu, J.B.H., Wu, Y.-M., Chang, C.-H., Chen, Y.-G., 2012. Seismotectonics of northeastern Taiwan: Kinematics of the transition from waning subduction and post-collisional extension. J. Geophys. Res. 117, B01313.

Huang, S.Y., Yen, J.Y., Wu, B.L., Yen, I.C., Chuang, R.Y., 2019. Investigating the Milun Fault: the coseismic surface rupture zone of the 2018/02/06 M_L 6.2 Hualien earthquake, Taiwan. Terr. Atmos. Ocean. Sci. 30, 311–335.

Kao, H., Shen, S.S.J., Ma, K.F., 1998. Transition from oblique subduction to collision: Earthquakes in the southernmost Ryukyu arc-Taiwan region. J. Geophys. Res. 103, 7211–7229.

Kuochen, H., Wu, Y.M., Chang, C.H., Hu, J.C., Chen, W.S., 2004. Relocation of eastern Taiwan earthquakes and tectonic implications. Terr. Atmos. Ocean. Sci. 15, 647–666.

Lallemand, S., Font, Y., Bijwaard, H., Kao, H., 2001. New insights on 3-D plates interaction near Taiwan from tomography and tectonic implications. Tectonophysics 335 (3–4), 229–253.

Lee, J.C., Angelier, J., Chu, H.-T., Yu, S.B., Hu, J.C., 1998. Plate boundary strain partitioning along the sinistral collision suture of the Philippine and Eurasian plates: Analysis of geodetic data and geological observation in southeastern Taiwan. Tectonics 17, 859–871.

Lee, J.-C., Angelier, J., Chu, H.-T., Hu, J.-C., Jeng, F.-S., 2001. Continuous monitoring of an active fault in a plate suture zone: a creepmeter study of the Chihshang fault, eastern Taiwan. Tectonophysics 333, 219–240.

Lee, S.-J., Lin, T.-C., Liu, T.-Y., Wong, T.-P., 2019. Fault-to-Fault jumping Rupture of the 2018 MwMw 6.4 Hualien Earthquake in Eastern Taiwan. Seismol. Res. Lett. 90 (1), 30–39.

Liao, H.S., 2006. Study of Milun Fault by using Shallow Reflection Seismic. MA thesis, 82 pp. Natl Chung Cheng Univ., Chiayi (in Chinese).

Lin, C.C., 1962. The Quaternary of the Hualien Area - the Quaternary of Taiwan. National Council on Science Development Research Report. 42 pp. (in Chinese).

Lin, C.-C., 1957. Geomorphology of Taiwan. Taiwan Prov. Lit. Comm., Taipei, 424 pp. (in Chinese).

Lin, M.S., Hsiao, C.L., 1998. The strike-slip fault system in the Milun Tableland. Res. of Eastern Taiwan 3, 13–30 (in Chinese).

Lin, Y.-S., Chuang, R.Y., Yen, J.-Y., Chen, Y.-C., Kuo, Y.-T., Wu, B.-L., Huang, S.-Y., Yang, C.-J., 2019. Mapping surface breakages of the 2018 Hualien earthquake by using UAS photogrammetry. Terr. Atmos. Ocean. Sci. 30, 351–366.

Liu, C.-S., Liu, S.-Y., Lallemand, S.E., Lundberg, N., Reed, D.L., 1998. Digital elevation model offshore Taiwan and its tectonic implications. Terr. Atmos. Ocean. Sci. 9, 705–738.

Malavieille, J., Lallemand, S.E., Dominguez, S., Deschamps, A., Lu, C.-Y., Liu, C.-S., Schnürle, P., 2002. Arc-continent collision in Taiwan: New marine observations and tectonic evolution. In: Byrne, T.B., Liu, C.-S. (Eds.), Geology and Geophysics of an Arc-Continent Collision, Taiwan, Republic of China: Boulder, Colorado, Geological Society of America Special Paper, vol. 358, pp. 189–213.

Shyu, J.B.H., Sieh, K., Chen, Y.G., Liu, C.S., 2005. Neotectonic architecture of Taiwan and its implications for future large earthquakes. J. Geophys. Res. 110, B08402.

Shyu, J.B.H., Chen, C.-F., Wu, Y.-M., 2016. Seismotectonic characteristics of the northernmost Longitudinal Valley, eastern Taiwan: Structural development of a vanishing suture. Tectonophysics 692, 295–308.

Shyu, J.B.H., Yin, Y.-H., Chen, C.-H., Chuang, Y.-R., Liu, S.-C., 2020. Updates to the on-land seismogenic structure source database by the Taiwan Earthquake Model (TEM) project for seismic hazard analysis of Taiwan. Terr. Atmos. Ocean. Sci. 31, 469–478 doi: 10.3319/TAO.2020.06.08.01.

Sibuet, J.-C., Hsu, S.-K., 2004. How was Taiwan created? Tectonophysics 379, 159–181.

Sibuet, J.-C., Deffontaines, B., Hsu, S.-K., Thareau, N., Le Formal, J.-P., Liu, C.-S., the ACT party, 1998. Okinawa Trough backarc basin: early tectonic and magnetic evolution. J. Geophys. Res. 103, 30245–30267.

Teng, L.S., 1990. Geotectonic evolution of late Cenozoic arc-continent collision in Taiwan. Tectonophysics 183, 57–76.

Theunissen, T., Lallemand, S., Font, Y., Gautier, S., Lee, C.-S., Liang, W.-T., Wu, F., Berthet, T., 2012. Crustal deformation at the southernmost part of the Ryukyu subduction (East Taiwan) as revealed by new marine seismic experiments. Tectonophysics 578, 10–30.

Tseng, Y.Z., 2019. Paleoseismic Study of Milun Active Fault in Hualien, eastern Taiwan. MA Thesis, 154 pp. Natl Central Univ., Taoyuan (in Chinese).

Wang, S.-Y., Hsu, S.-K., Yeh, Y.-C., 2019. Earthquake-related structures beneath the southernmost portion of the Ryukyu arc and forearc. Geophys. Res. Lett. 46 (7), 3717–3725.

Wu, F.T., Liang, W.T., Lee, J.C., Benz, H., Villasenor, A., 2009a. A model for the termination of the Ryukyu subduction zone against Taiwan: a junction of collision, subduction/separation, and subduction boundaries. J. Geophys. Res. Solid Earth 114 (B7).

Wu, Y.M., Chang, C.H., Zhao, L., Teng, T.L., Nakamura, M., 2008. A Comprehensive Relocation of Earthquakes in Taiwan from 1991 to 2005. Bull. Seismol. Soc. Am. 98 (3), 1471–1481.

Wu, Y.M., Shyu, J.B.H., Chang, C.H., Zhao, L., Nakamura, M., Hsu, S.K., 2009b. Improved seismic tomography offshore northeastern Taiwan: Implications for subduction and collision processes between Taiwan and the southernmost Ryukyu. Geophys. J. Int. 178, 1042–1054.

Yang, G.-S., 1986. A geomorphological study of active faults in Taiwan—Especially on the relation between active faults and geomorphic surfaces. Ph.D. thesis, 178 pp. Chin. Culture Univ., Taipei (in Chinese).

Yang, Y.-C., 1953. Earthquakes in Hualien in the latest 41 years. Hualien Lit. 1, 67–71 (in Chinese).

Yen, J.-Y., Lu, C.-H., Chang, C.-P., Hooper, A.J., Chang, Y.-H., Liang, W.-T., Chang, T.-Y., Lin, M.-S., Chen, K.-S., 2011. Investigating active deformation in the northern Longitudinal Valley and City of Hualien in eastern Taiwan using persistent scatterer and smallbaseline SAR interferometry. Terr. Atmos. Ocean. Sci. 22, 291–304.

Yen, J.-Y., Lu, C.-H., Dorsey, R.-J., KuoChen, H., Chang, C.-P., Wang, C.-C., Chuang, Y., Kuo, Y.-T., Chiu, C.-Y., Chang, Y.-H., Bovenga, F., Chang, W.-Y., 2019. Insights into Seismogenic Deformation during the 2018 Hualien, Taiwan, Earthquake Sequence from InSAR, GPS, and Modeling. Seismol. Res. Lett. 90 (1), 78–87.

Yu, M.S., 1994. Wrench-fault characteristics of the Taitung Longitudinal Valley Fault zone. Ti-Chih 14, 121–147 (in Chinese).

Yu, M.-S., 1997. Active Faults in the Taitung Longitudinal Valley. Ph.D. Thesis, 141 pp. Natl. Taiwan Univ., Taipei (in Chinese).

Yu, S.-B., Kuo, L.-C., 2001. Present-day crustal motion along the Longitudinal Valley Fault, eastern Taiwan. Tectonophysics 333, 199–217.

Yu, S.B., Jackson, D.D., Yu, G.K., Liu, C.C., 1990. Dislocation model for crustal deformation in the Longitudinal Valley area, eastern Taiwan. Tectonophysics 183, 97–109.

Yu, S.-B., Chen, H.-Y., Kuo, L.-C., 1997. Velocity field of GPS stations in the Taiwan area. Tectonophysics 274, 41–59.